

Quantum-confined bismuth iodide perovskite nanocrystals in mesoporous matrices

Sarah Dupé, Dongyu Liu, Antik Ghosh, Andrey S. Vasenko, Stéphanie Pouget, Sandrine Schlutig, Mathieu Vidal, Bénédicte Lebeau, Wai Li Ling, Peter Reiss, Oleg V. Prezhdo, Andrey Ryzhikov, Dmitry Aldakov*

S. Dupé (sarahdupe@icloud.com), A. Ghosh (antik.ghosh@cea.fr), P. Reiss (peter.reiss@cea.fr), D. Aldakov (dmitry.aldakov@cea.fr)
Univ. Grenoble Alpes, CNRS, CEA, INP, IRIG/SyMMES, STEP, 38000 Grenoble, France

D. Li (dongyu.liu@qq.com)
International Research Center for Renewable Energy (IRCRES), State Key Laboratory of Multiphase Flow in Power Engineering (MFPE), Xi'an Jiaotong University, Xi'an, Shaanxi 710049, China

A. S. Vasenko (andrey.vasenko@lpmmc.cnrs.fr)
Donostia International Physics Center (DIPC), 20018 San Sebastián-Donostia, Euskadi, Spain

S. Pouget (stephanie.pouget@cea.fr), S. Schlutig (sandrine.schlutig@cea.fr)
Univ. Grenoble Alpes, CEA Grenoble, IRIG, MEM, SGX, Grenoble, France

M. Vidal (mathieu.vidal@lcc-toulouse.fr), B. Lebeau (benedicte.lebeau@uha.fr), A. Ryzhikov (andrey.ryzhikov@uha.fr)
Université de Haute-Alsace, CNRS, Institut de Science des Matériaux de Mulhouse (IS2M), UMR 7361, Axe Matériaux à Porosité Contrôlée, F-68100, Mulhouse, France; Université de Strasbourg, F-67000 Strasbourg, France

W. L. Ling (wai-li.ling@ibs.fr)
Univ. Grenoble Alpes, CEA, CNRS, IBS, 38000 Grenoble, France

O. V. Prezhdo (prezhdo@usc.edu)
Department of Chemistry and Department of Physics & Astronomy, University of Southern California, Los Angeles, California 90089, United States

Supporting information

Experimental part

Chemicals

Cesium iodide (CsI, 99.9%, Alfa Aesar), methylammonium iodide (MAI, GreatCellSolar), bismuth iodide (BiI₃, 99.999%, Strem), N,N-dimethylformamide (DMF, anhydrous, 99.8%, Aldrich), dimethylsulfoxide (DMSO, anhydrous, 99.5%, Aldrich) were used as received.

Synthesis of mesoporous silica

SBA-15 and MCM-41 mesoporous silica have hexagonal pore system with unidimensional mesopores. In the case of SBA-15, the mesopores are connected by some micropores, whereas MCM-41

mesopores are not connected. SBA-15 (pore size of 7.4 and ~9.2 nm) and MCM-41 (pore size 2.3 and 3.7 nm) mesoporous silicas have been obtained according the following procedures. To obtain SBA-15 samples, the triblock copolymer Pluronic P123 [(EO)₂₀-(PO)₇₀-(EO)₂₀, BASF] was used as a pore-templating agent. To obtain the sample with pore diameter of 7.4 nm, in a polypropylene bottle, P123 (4 g) was dissolved in an acidic medium of concentrated hydrochloric acid and water (23.28 g of HCl 37% (SigmaAldrich) in 127 mL of demineralized water) during 2 hours at 40°C, when 9.1 mL (8.55 g) of tetraethoxysilane (TEOS, SigmaAldrich) was added. The mixture was stirred at 35°C during 4 hours, then heated at 95°C for 24 hours under static conditions.¹ To obtain the SBA-15 with pore diameter of 9.2 nm, NH₄F (0.046 g, SigmaAldrich) was added to the solution of P123 (4.0 g) in 19.5 mL of HCl 37% (SigmaAldrich) mixed with 127 mL of water.² The solution was then stirred for 3 hours at 40°C, then 8.62 g of TEOS was added and stirred for 24 hours at 40°C. Then, the mixture was heated at 90°C for 24 hours at static conditions.

To obtain MCM-41 samples, cetyltrimethylammonium bromide (CTAB, Fluka) was used as a pore-templating agent. To synthesize MCM-41 with pore diameter of 2.3 nm, 1.75 g of CTAB was dissolved in NaOH solution in demineralized water (0.368 g in 93.6 mL, respectively) at 40°C under stirring. Then 8.35 g of TEOS was added dropwise and the mixture was stirred at 40°C for 66 hours. To obtain MCM-41 with pore diameter of 3.7 nm, 1.46 g of CTAB was added to 14 mL of demineralized water under stirring, then 8.47 g of 10% tetramethylammonium hydroxide solution (TMAOH, Fluka) was added. Then 2 g of Aerosil 200 fumed silica (Degussa) was added. The mixture was stirred for 30 minutes, then transferred into a PTFE-lined stainless-steel autoclave and heated at 150°C for 4 days.³

In the end of every synthesis, the white powders were collected by filtration and washed with deionized water on a Büchner funnel, then dried at 70°C overnight. In order to remove the organic template, the powders were calcined at 500°C for 6 hours under air for the SBA-15 sample with pore diameter of 7.4 nm and at 300°C for 4 hours for the one 9.2 nm, whereas MCM-41 samples were calcined at 550°C for 12 hours.

Synthesis of perovskite nanocrystals in mesoporous matrices

0.7 M BiI₃ solution: 413 mg (0.7 mmol) of BiI₃ was dissolved in 800 µL DMF and 200 µL DMSO by using ultrasonication and stirring at 30°C overnight. 1.05 M MAI (CsI) solution: 167 mg (1.05 mmol) of MAI (or 273 mg, 1.05 mmol of CsI) was dissolved in 800 µL DMF and 200 µL DMSO. The two solutions were mixed together, stirred overnight and passed through a 0.2 µm PTFE filter. Different amounts of this MA₃Bi₂I₉ and Cs₃Bi₂I₉ precursor solutions (25, 50, and 100 µL) were added to 100 mg SBA-15 or MCM-41 powders (dried under vacuum at 100°C overnight). The obtained yellow-orange powder was vortex-mixed for 1 h followed by the annealing in an oven at 100°C under argon.

Characterization techniques

Optical absorption spectroscopy was performed on Perkin Elmer Lambda 950 UV-vis-NIR spectrophotometer: the powders were dispersed between two glass slides and measured in a transmission mode using integrating sphere. X-ray diffraction patterns of powders in capillaries were recorded on a Bruker D8 diffractometer using Cu-Kα (λ = 1.5406 Å) radiation. Scanning and scanning transmission electron microscopy were operated on a Zeiss Ultra 55 microscope. EDX spectroscopy was carried out on the above-mentioned microscope using working distance of 7 mm. Transmission electron microscopy was performed on Philips CM200 microscope. Nitrogen adsorption-desorption isotherms at -196°C were obtained using a Micromeritics Tristar apparatus. Prior to the adsorption measurements, the samples were outgassed at 120°C overnight under vacuum. The specific surface area (S_{BET}) and microporous volume (V_{micro}) were calculated using the BET and t-plot methods, respectively. Mesopore diameter values were calculated from desorption branch of isotherm using

Broekhoff and de Boer (BdB) method. XPS was carried out using a Versaprobe II ULVAC-PHI spectrometer in an ultra-high vacuum chamber (7.10^{-8} mbar) equipped with a monochromated Al K α source (1486.6 eV). The core-level peaks were recorded with a constant pass energy of 23.3 eV. Binding energies are referenced with respect to adventitious carbon (284.8 eV). 30/70 Gaussian-Lorentzian peak models with Shirley backgrounds were used to fit the data using Casa XPS software. ICP-OES measurements were performed on a Shimadzu 9000 spectrometer. The samples were prepared by dissolving powders in 10% HNO₃. Standards solutions of the metal ions were prepared by diluting Bi and Si ICP standards with HNO₃ 10% (v/v). Subsequently, calibration curves were established for the concentration range relevant to our samples. X-ray diffractograms were measured using a Bruker D8 Discover model with copper source ($\lambda=1.54$ Å). The data was measured in capillary mode using a divergence slit of 1 mm and an air scatter to reduce the signal-to-noise ratio for a high resolution diffractogram. The samples were prepared in ambient atmosphere using a Kapton capillary tube of the diameter around 1.14 mm. Lanthanum hexaborate (LaB₆) was used as a blank data in the Kapton capillaries before the sample measurements to get rid of the instrumentation errors while refining the sample data.

All DFT calculations were performed using the Vienna *Ab initio* Simulation Package (VASP).⁴⁻⁷ The projector augmented-wave (PAW)⁸ method and the Perdew–Burke–Ernzerhof (PBE) functional⁹ were adopted for electronic structure calculations. We tested different functionals and found only PBE and HSE06¹⁰ with spin-orbit coupling (SOC) can produce reasonable bandgap results (see Figure S14), which is consistent with previous work.¹¹ The HSE06 hybrid functional with SOC is not taken into account because it is much more costly than PBE. The cutoff energy of the plane wave basis was set to 250 eV.¹² A Gaussian smearing with a σ of 0.05 eV was used. We took the structure of hexagonal Cs₃Bi₂I₉ unit cell from the Materials Project database without further optimization.¹³ The bulk properties were calculated using the unit cell with a $3\times 3\times 1$ *k*-points mesh. In addition to the electronic structure, the absorption spectrum was simulated by solving the Bethe–Salpeter equation (BSE). The screened Coulomb kernel was calculated with the *GW*₀ method, where 640 bands were used and *G* was iterated four times. All the occupied orbitals (100 orbitals) and 80 unoccupied orbitals were included in the solution of the BSE. To study the quantum confinement effects, we constructed cylinder models of Cs₃Bi₂I₉ by adding vacuum region in the *x* and *y* directions while maintain the extended periodic structure in the *z* direction (see Figure S17). The diameter of the cylinder models was changed to investigate the dependence of the experimental bandgap on the pore size. Only the gamma point was used to sample the Brillouin zone here. These models were not optimized, and there are many surface states near the band edges owing to the unsaturated atoms. We calculated the corresponding bandgap after manually removing some localized surface states which should be passivated by the interactions between the Cs₃Bi₂I₉ quantum dots and the mesoporous silica matrices in the experiment (Figures S18-S20). The structures were visualized using the VESTA software package,¹⁴ and the calculated results were postprocessed with the VASPKIT code.¹⁵

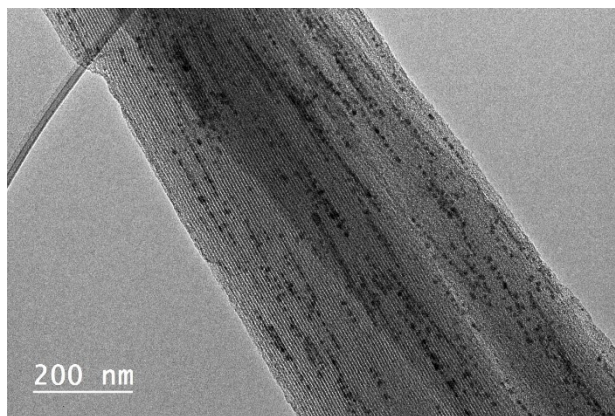


Figure S1. TEM image of MA₃Bi₂I₉@SBA-15 (7.2 nm pore diameter, 7.3 mass. %).

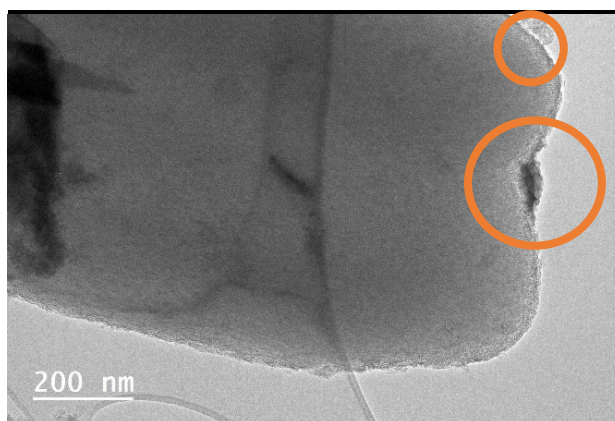


Figure S2. TEM image of MA₃Bi₂I₉@MCM-41 (3.7 nm pore diameter, 14.5 mass. %) highlighting possible locations of the MA₃Bi₂I₉ crystals outside of the pores.

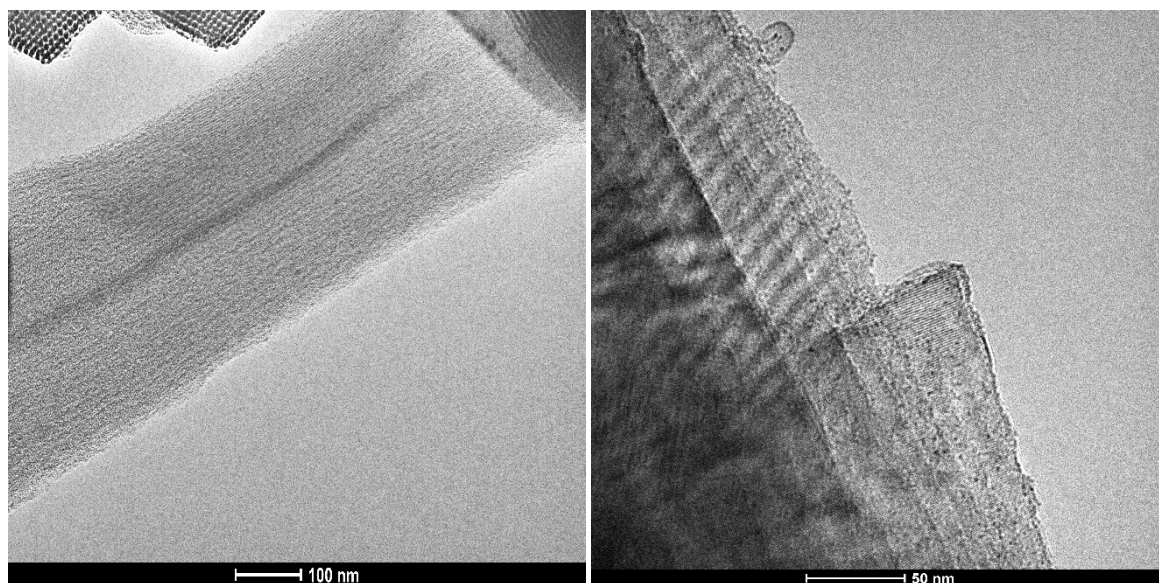


Figure S3. TEM images of Cs₃Bi₂I₉@SBA-15 (7.2 nm pore diameter, 14.5 mass. %).

Table S1. Textural properties of MA₃Bi₂I₉@SBA-15 (7.4 nm) samples: BET surface area (S_{BET}), micropore (V_{micro}), mesopore (V_{meso}) and total (V_{total}) pore volumes.

MA ₃ Bi ₂ I ₉ @SBA-15 (7.4 nm), mass. %	S_{BET} , m ² /g	V_{micro} , cm ³ /g	V_{meso} , cm ³ /g	V_{total} , cm ³ /g
0	828	0.17	0.70	0.90
7.3	485	0.07	0.58	0.67
14.5	500	0.07	0.58	0.67
29	406	0.04	0.51	0.57

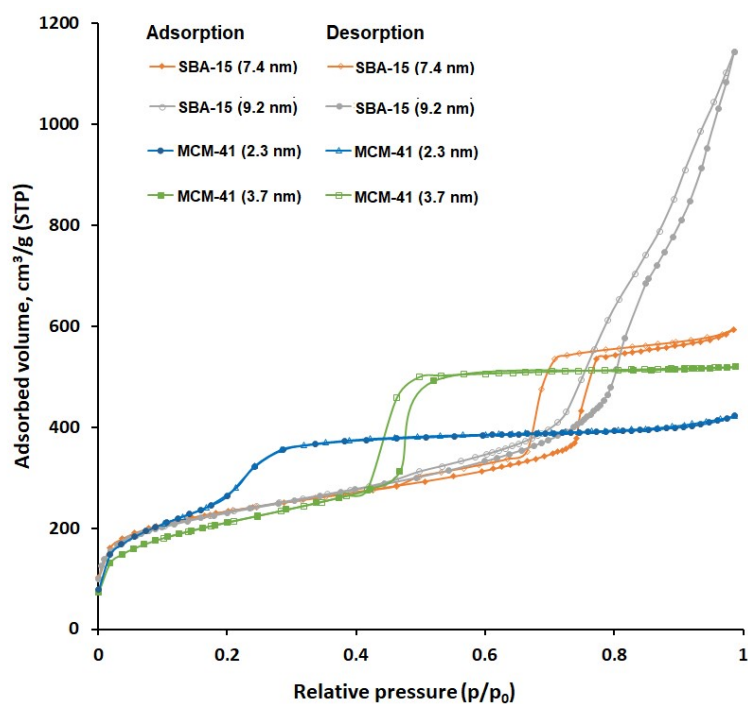


Figure S4. Nitrogen adsorption-desorption isotherms at -196°C for MCM-41 and SBA-15 samples.

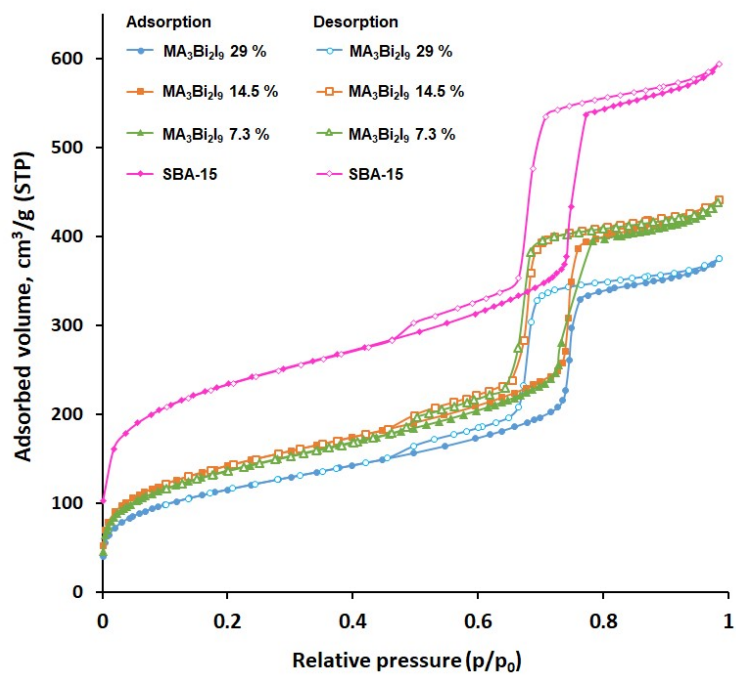


Figure S5. Nitrogen adsorption-desorption isotherms at -196°C for $\text{MA}_3\text{Bi}_2\text{I}_9@$ SBA-15 samples (7.4 nm pore diameter).

Table S2. Textural properties of MCM-41 and SBA-15 samples: BET surface area (S_{BET}), micropore (V_{micro}), mesopore (V_{meso}) and total (V_{total}) pore volumes.

Silica type	Mesopore diameter, nm	S_{BET} , m^2/g	V_{micro} , cm^3/g	V_{meso} , cm^3/g	V_{total} , cm^3/g
MCM-41	2.3	883	-	0.60	0.64
MCM-41	3.7	759	-	0.79	0.80
SBA-15	7.4	828	0.17	0.70	0.90
SBA-15	9.2	793	0.12	1.11	1.74

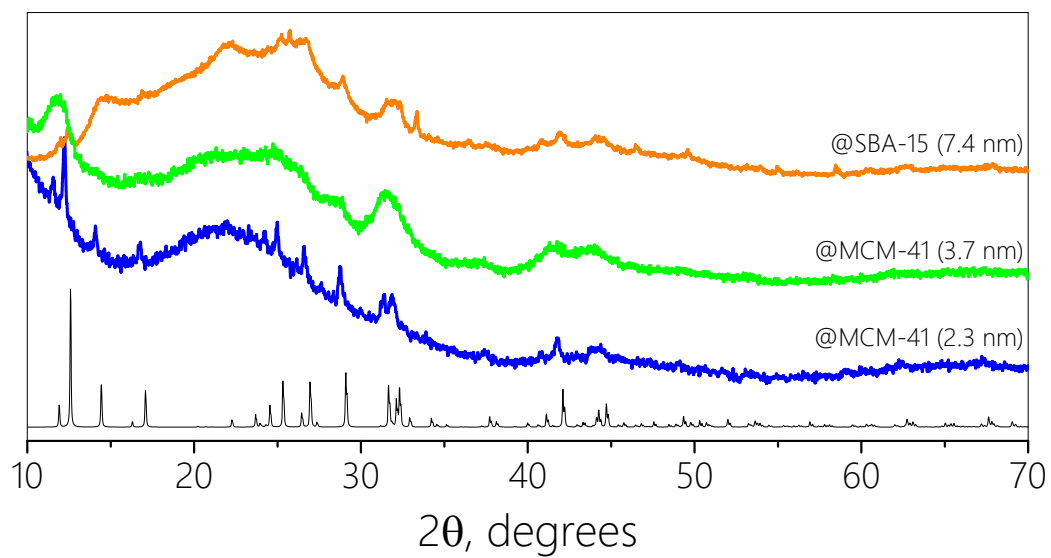


Figure S6. XRD pattern of MA₃Bi₂I₉ encapsulated in various mesoporous matrices (14.5 mass. %). Reference (black line): ICDD 01-085-6014. Refinement: monoclinic, C2/c, a=8.7 b=14.8 c=21.51 β: 91.43

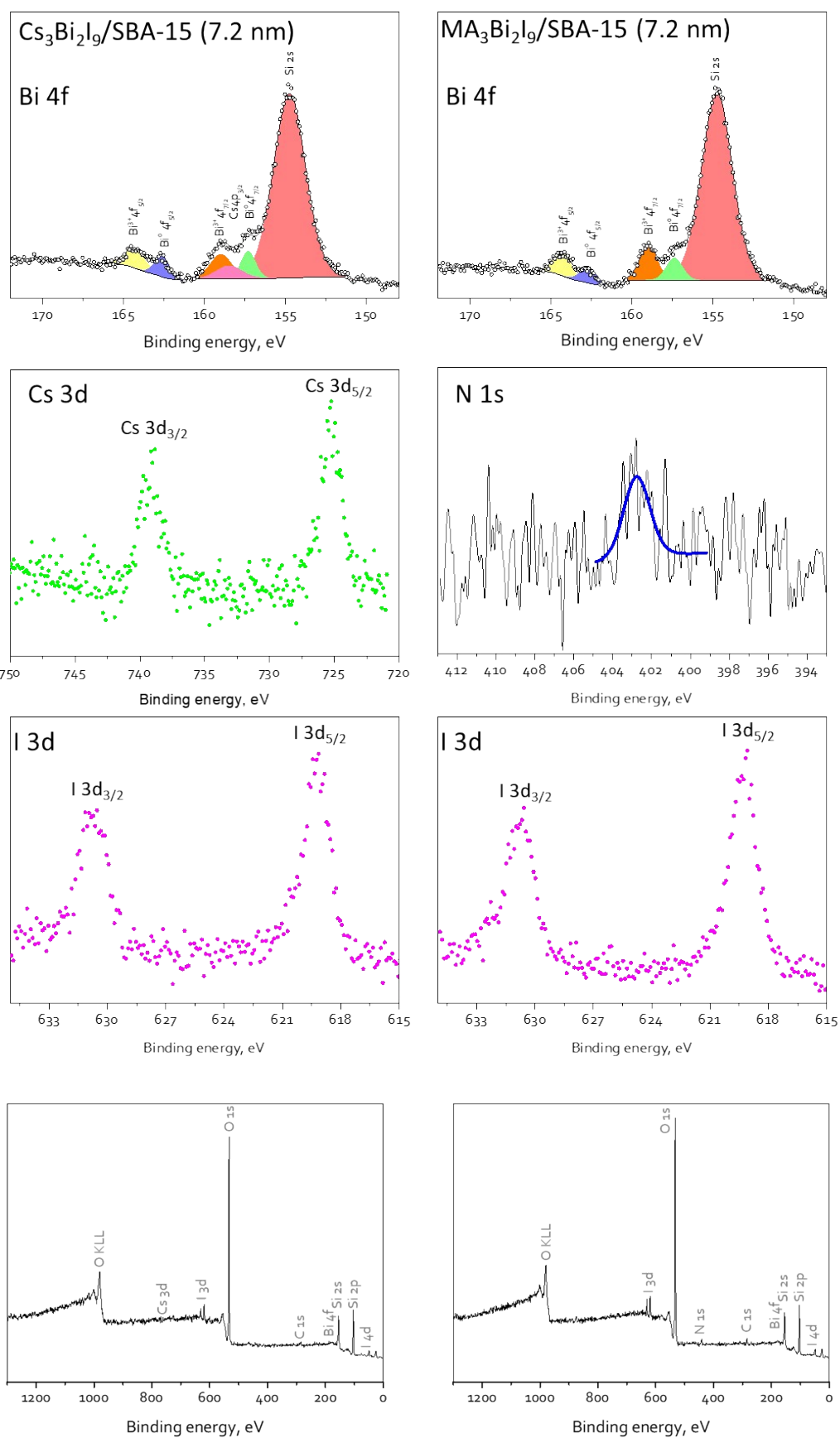


Figure S7. XPS spectra of $\text{Cs}_3\text{Bi}_2\text{I}_9$ (left column) and $\text{MA}_3\text{Bi}_2\text{I}_9$ (right column) @SBA-15 (7.2 nm, 14.5 mass. %)

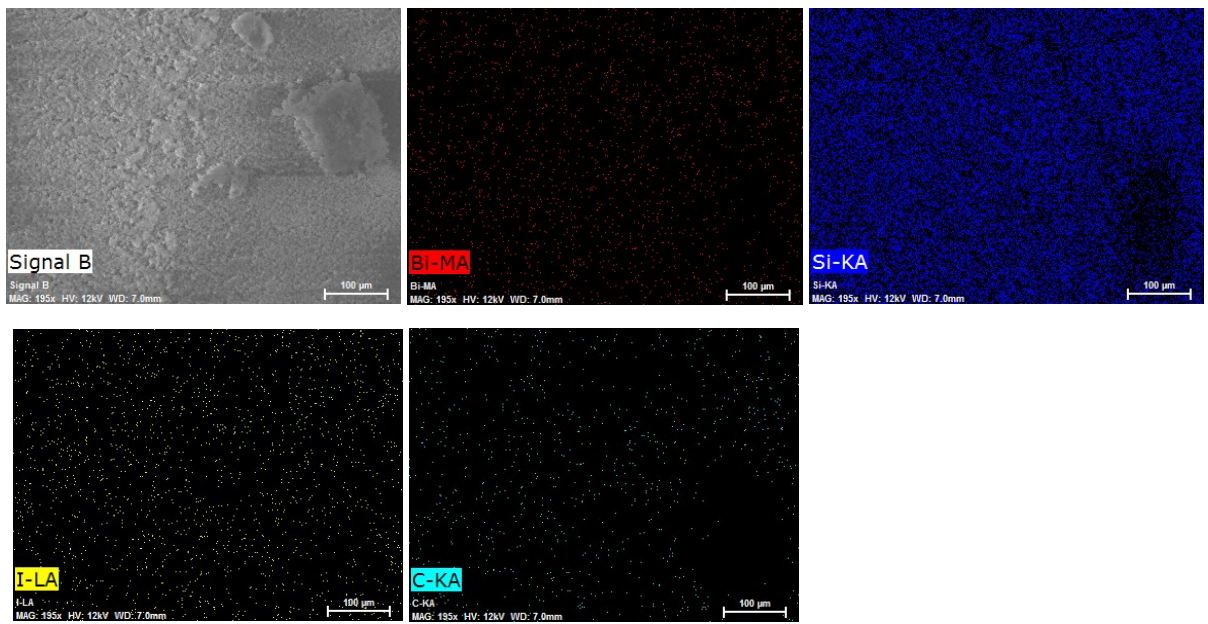


Figure S8. EDX mapping of $MA_3Bi_2I_9@SBA-15$ (7.2 nm, 14.5 mass. %)

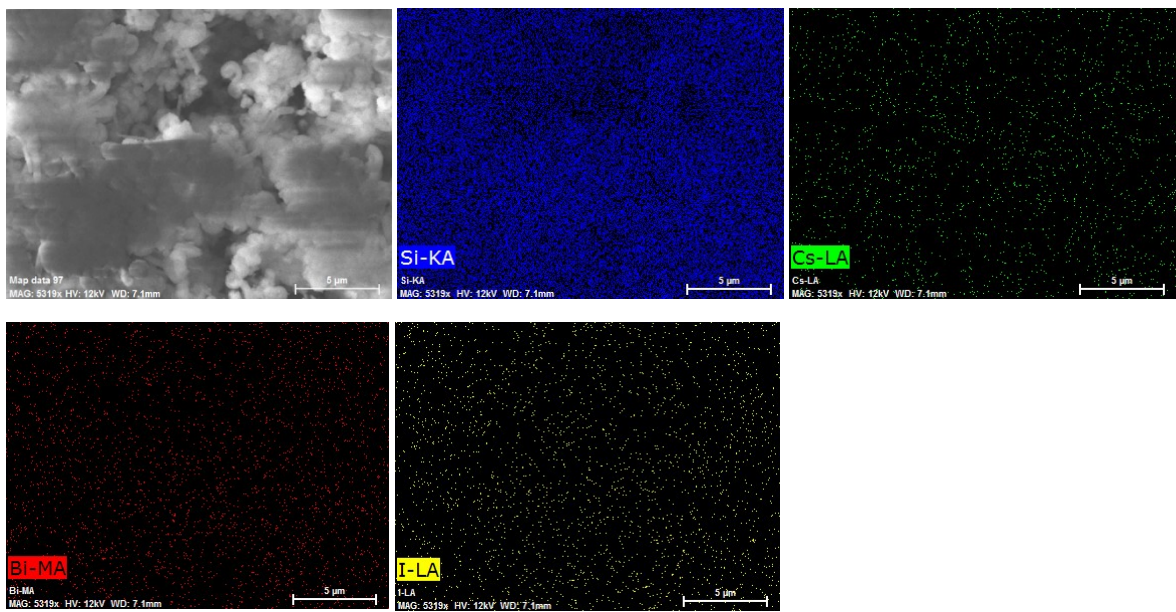
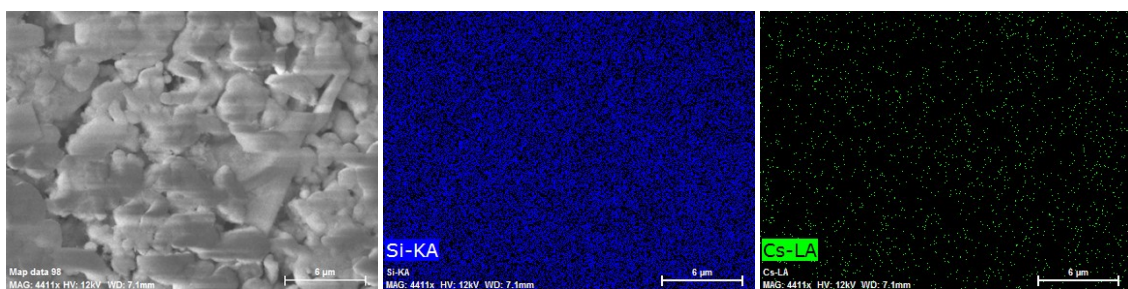


Figure S9. EDX mapping of $Cs_3Bi_2I_9@SBA-15$ (7.2 nm, 14.5 mass. %)



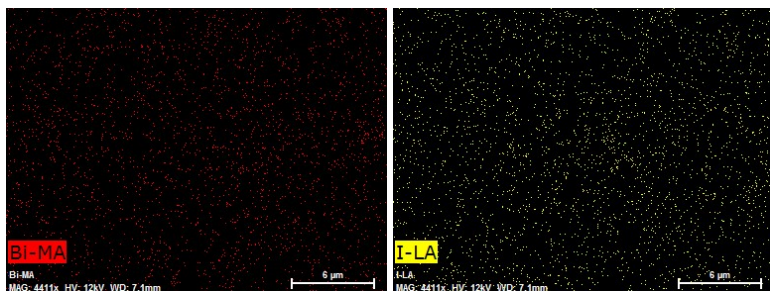


Figure S10. EDX mapping of $\text{Cs}_3\text{Bi}_2\text{I}_9$ @MCM-41 (2.3 nm, 14.5 mass. %)

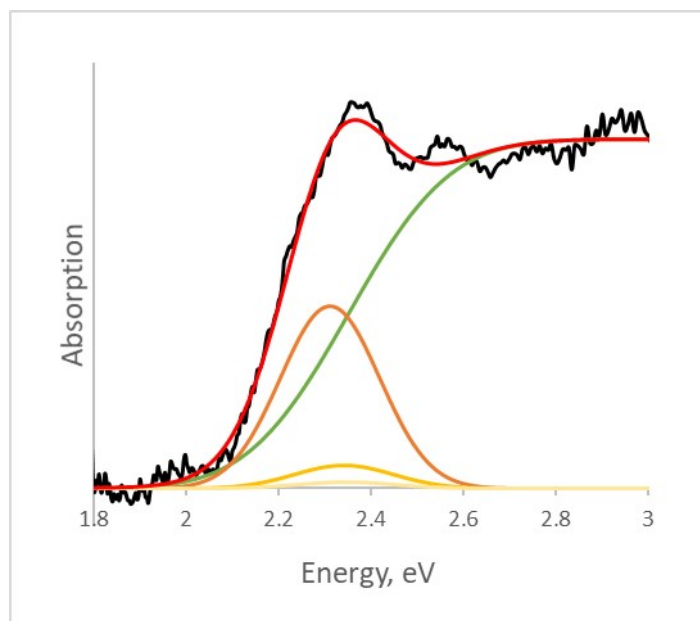


Figure S11. Absorption spectrum of $\text{Cs}_3\text{Bi}_2\text{I}_9$ @MCM-41 (2.3 nm, 7.3 mass. %) (black) tentatively fitted with a only single Elliott curve (red). One can see its constituents: the continuum curve (green), as well as three excitonic peaks (shades of orange).

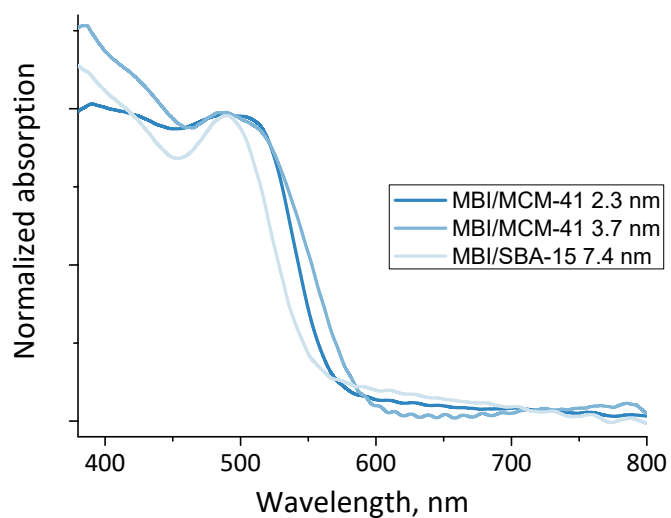


Figure S12. Absorption spectra of powders of $\text{MA}_3\text{Bi}_2\text{I}_9$ (14.5 mass. %) encapsulated in various mesoporous matrices

Table S3. Bandgap dependence of the encapsulated $MA_3Bi_2I_9$ on the silica matrix pore size

Pore size	E_g 1, eV	E_b 1, meV	E_g 2, eV	E_b 2, meV
2.3 nm	2.54	80	2.68	330
3.7 nm	2.58	110	2.66	340
7.4 nm	2.59	170	2.67	150

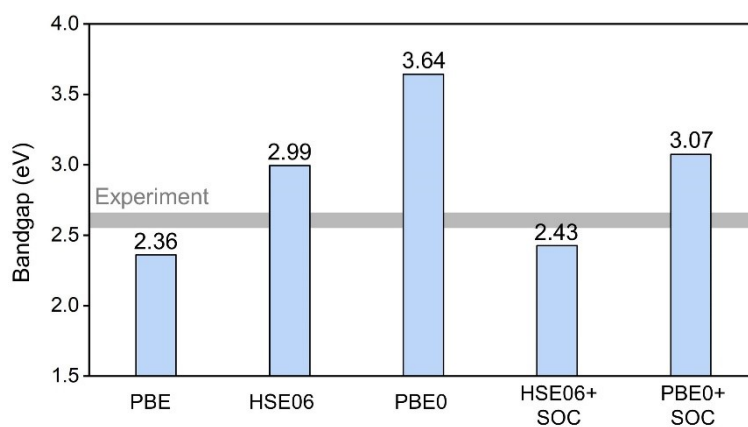


Figure S13. Comparison of the calculated bandgap of $Cs_3Bi_2I_9$ with different functionals

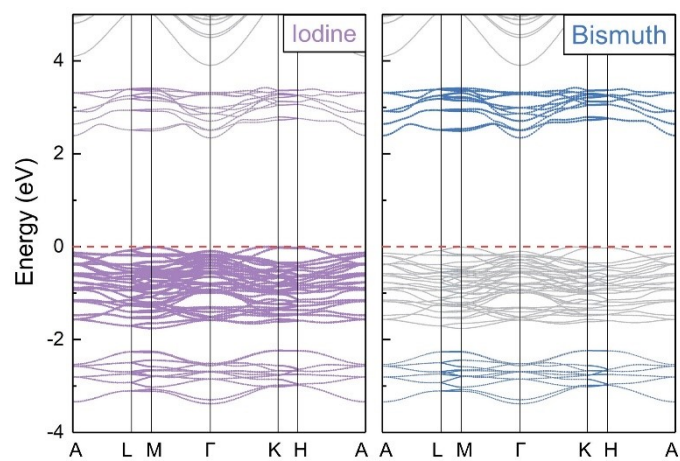


Figure S14. Element-projected band structure. The size of the dots represents the contribution of each element to the states.

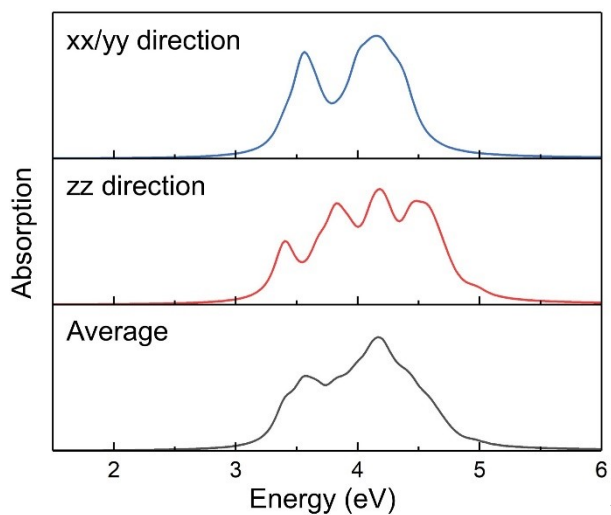


Figure S15. Raw data of the calculated optical absorption spectra.

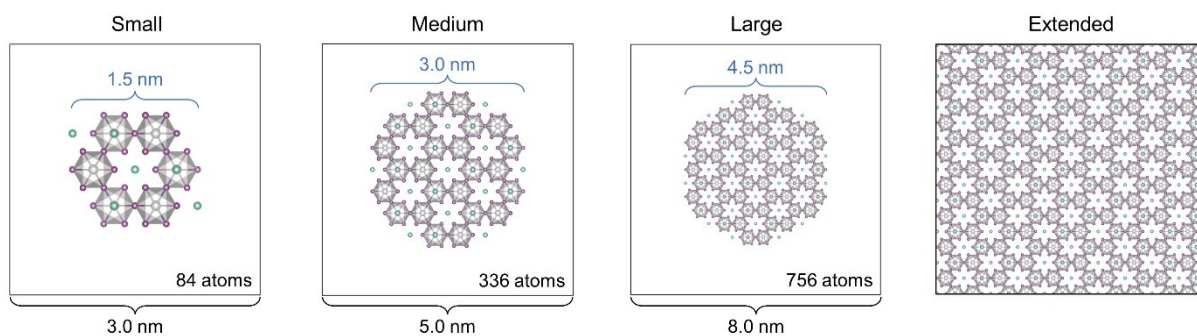


Figure S16. Top view of different quantum dot models and the periodic model.

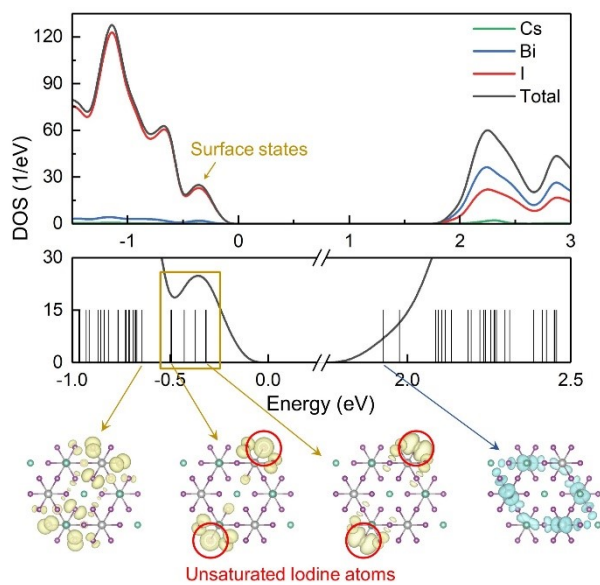


Figure S17. DOS of the small quantum dot model and the elimination of the surface states.

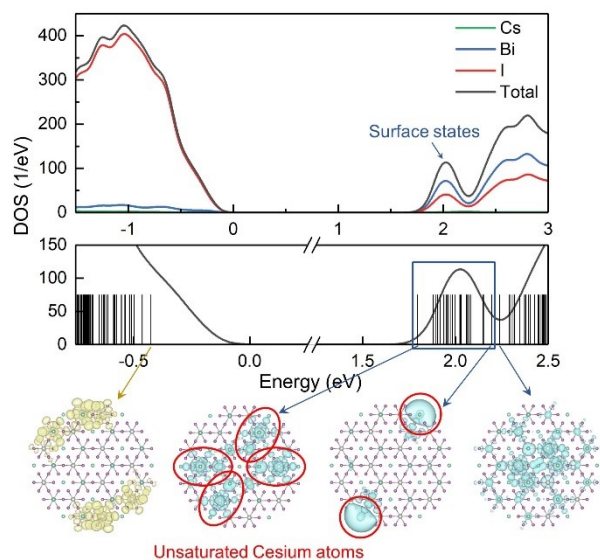


Figure S18. DOS of the medium quantum dot model and the elimination of the surface states.

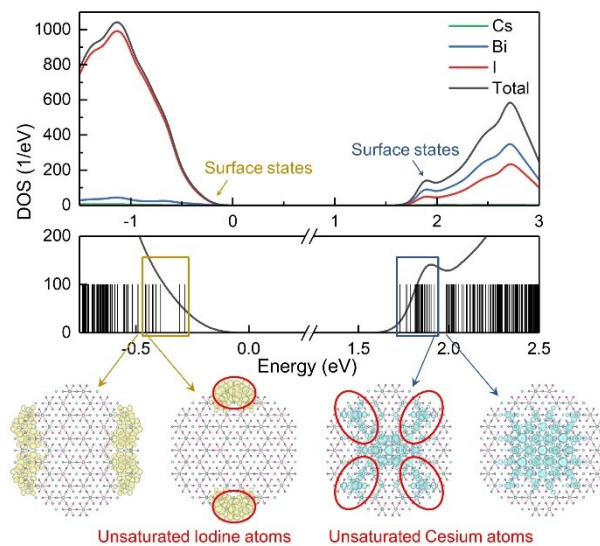


Figure S19. DOS of the big quantum dot model and the elimination of the surface states.

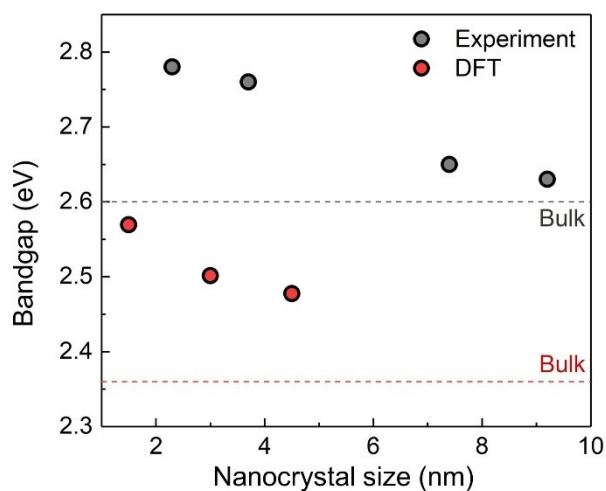


Figure S20. Raw data of the experimental the computational bandgap results.

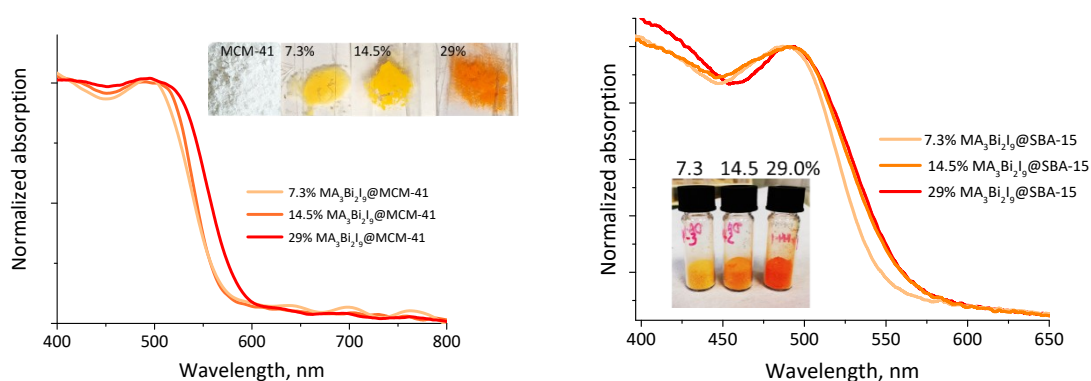


Figure S21. Absorption spectra of powders of $\text{MA}_3\text{Bi}_2\text{I}_9$ @MCM-41 (2.3 nm pore size, left) and @SBA-15 (7.4 nm pore size, right) with different loadings

Table S4. Influence of the perovskite loading on the bandgaps

$\text{MA}_3\text{Bi}_2\text{I}_9$ @MCM-41	E_g 1, eV	E_g 2, eV	β_1/β_2
7.3%	2.50	2.65	0.08
14.5%	2.55	2.69	0.86
29%	2.45	2.61	2.40

References

- 1 D. Zhao, Q. Huo, J. Feng, B. F. Chmelka and G. D. Stucky, *J. Am. Chem. Soc.*, 1998, **120**, 6024–6036.
- 2 P. Schmidt-Winkel, P. Yang, D. I. Margolese, B. F. Chmelka and G. D. Stucky, *Adv. Mater.*, 1999, **11**, 303–307.

- 3 A. C. Voegtlin, A. Matijasic, J. Patarin, C. Sauerland, Y. Grillet and L. Huve, *Microporous Mater.*, 1997, **10**, 137–147.
- 4 G. Kresse and J. Furthmüller, *Comput. Mater. Sci.*, 1996, **6**, 15–50.
- 5 G. Kresse and J. Furthmüller, *Phys. Rev. B*, 1996, **54**, 11169–11186.
- 6 G. Kresse and J. Hafner, *Phys. Rev. B*, 1994, **49**, 14251–14269.
- 7 G. Kresse and J. Hafner, *Phys. Rev. B*, 1993, **47**, 558–561.
- 8 P. E. Blöchl, *Phys. Rev. B*, 1994, **50**, 17953–17979.
- 9 J. P. Perdew, K. Burke and M. Ernzerhof, *Phys. Rev. Lett.*, 1996, **77**, 3865–3868.
- 10 A. V Krukau, O. A. Vydrov, A. F. Izmaylov and G. E. Scuseria, *J. Chem. Phys.*, 2006, **125**, 224106.
- 11 B. Ghosh, S. Chakraborty, H. Wei, C. Guet, S. Li, S. Mhaisalkar and N. Mathews, *J. Phys. Chem. C*, 2017, **121**, 17062–17067.
- 12 Y. Xie, B. Peng, I. Bravić, Y. Yu, Y. Dong, R. Liang, Q. Ou, B. Monserrat and S. Zhang, *Adv. Sci.*, 2020, **7**, 2001698.
- 13 A. Jain, S. P. Ong, G. Hautier, W. Chen, W. D. Richards, S. Dacek, S. Cholia, D. Gunter, D. Skinner, G. Ceder and K. A. Persson, *APL Mater.*, 2013, **1**, 11002.
- 14 K. Momma and F. Izumi, *J. Appl. Crystallogr.*, 2011, **44**, 1272–1276.
- 15 V. Wang, N. Xu, J.-C. Liu, G. Tang and W.-T. Geng, *Comput. Phys. Commun.*, 2021, **267**, 108033.